IOP Publishing Phys. Med. Biol. 65 (2020) 025010 (16pp) https://doi.org/10.1088/1361-6560/ab58fa

Physics in Medicine & Biology

IPEM Institute of Physics and Engineering in Medicine

PAPER

RECEIVED
14 June 2019

REVISED
14 November 2019

ACCEPTED FOR PUBLICATION
19 November 2019

PUBLISHED
16 January 2020

Arterial wall mechanical inhomogeneity detection and atherosclerotic plaque characterization using high frame rate pulse wave imaging in carotid artery disease patients *in vivo*

Grigorios M Karageorgos[1,5], Iason Z Apostolakis[1,5], Pierre Nauleau[1], Vittorio Gatti[1], Rachel Weber[1], E Sander Connolly[2], Eliza C Miller[3] and Elisa E Konofagou[1,4,6]

[1] Department of Biomedical Engineering, Columbia University, New York, NY, United States of America
[2] Department of Neurological Surgery, Columbia University Irving Medical Center, New York, NY, United States of America
[3] Department of Neurology, Columbia University Irving Medical Center, New York, NY, United States of America
[4] Department of Radiology, Columbia University Irving Medical Center, New York, NY, United States of America
[5] Grigorios M Karageorgos and Iason Z Apostolakis contributed equally to this work.
[6] Author to whom any correspondence should be addressed.

E-mail: ek2191@columbia.edu

Keywords: pulse wave imaging, carotid artery disease, arterial wall stiffness, mechanical inhomogeneity, atherosclerosis

Abstract

Pulse wave imaging (PWI) is a non-invasive, ultrasound-based technique, which provides information on arterial wall stiffness by estimating the pulse wave velocity (PWV) along an imaged arterial wall segment. The aims of the present study were to: (1) utilize the PWI information to automatically and optimally divide the artery into the segments with most homogeneous properties and (2) assess the feasibility of this method to provide arterial wall mechanical characterization in normal and atherosclerotic carotid arteries *in vivo*. A silicone phantom consisting of a soft and stiff segment along its longitudinal axis was scanned at the stiffness transition, and the PWV in each segment was estimated through static testing. The proposed algorithm detected the stiffness interface with an average error of 0.98 ± 0.49 mm and 1.04 ± 0.27 mm in the soft-to-stiff and stiff-to-soft pulse wave transmission direction, respectively. Mean PWVs estimated in the case of the soft-to-stiff pulse wave transmission direction were 2.47 ± 0.04 m s^{-1} and 3.43 ± 0.08 m s^{-1} for the soft and stiff phantom segments, respectively, while in the case of stiff-to-soft transmission direction PWVs were 2.60 ± 0.18 m s^{-1} and 3.72 ± 0.08 m s^{-1} for the soft and stiff phantom segments, respectively, which were in good agreement with the PWVs obtained through static testing (soft segment: 2.41 m s^{-1}, stiff segment: 3.52 m s^{-1}). Furthermore, the carotid arteries of $N = 9$ young subjects (22–32 y.o.) and $N = 9$ elderly subjects (60–73 y.o.) with no prior history of carotid artery disease were scanned, *in vivo*, as well as the atherosclerotic carotid arteries of $N = 12$ (59–85 y.o.) carotid artery disease patients. One-way ANOVA with Holm-Sidak correction showed that the number of most homogeneous segments in which the artery was divided was significantly higher in the case of carotid artery disease patients compared to young (3.25 ± 0.86 segments versus 1.00 ± 0.00 segments, p-value < 0.0001) and elderly non-atherosclerotic subjects (3.25 ± 0.86 segments versus 1.44 ± 0.51 segments p-value < 0.0001), indicating increased wall inhomogeneity in atherosclerotic arteries. The compliance provided by the proposed algorithm was significantly higher in non-calcified/high-lipid plaques as compared with calcified plaques ($3.35 \pm 2.45 * 10^{-9}$ m^2 Pa^{-1} versus $0.22 \pm 0.18 * 10^{-9}$ m^2 Pa^{-1}, p-value < 0.01) and the compliance estimated in elderly subjects ($3.35 \pm 2.45 * 10^{-9}$ m^2 Pa^{-1} versus $0.79 \pm 0.30 * 10^{-9}$ m^2 Pa^{-1}, p-value < 0.01). Moreover, lower compliance was estimated in cases where vulnerable plaque characteristics were present (i.e. necrotic lipid core, thrombus), compared to stable plaque components (calcification), as evaluated through plaque histological examination. The proposed algorithm was thus capable of evaluating arterial wall inhomogeneity and characterize wall mechanical properties, showing promise in vascular disease diagnosis and monitoring.

1. Introduction

Carotid artery disease is a chronic vascular disease, characterized by the formation of atherosclerotic plaques in the carotid artery wall, causing progressive stenosis and impairing blood flow to the brain (Libby *et al* 2011). In case of plaque rupture, a blood clot may form, which may detach and transfer through the blood flow to smaller vessels in the brain, potentially leading to an ischemic stroke.

Current clinical tests mostly focus on the degree of stenosis, i.e. the percentage reduction in the luminal area of the vessel, in order to evaluate the risk for stroke (Grotta 2013). In case of severe carotid artery stenosis, and/or when the patient exhibits neurological symptoms, carotid endarterectomy or carotid stenting may be performed to partly or completely remove the atherosclerotic plaque. However, current tests have limitations, since low stenotic plaques may also rupture (Saam *et al* 2007). Furthermore, there is a need to develop more robust markers associated with sub-clinical atherosclerosis burden, in order to enable early prediction of cardiovascular events (Fernández-Ortiz *et al* 2013).

Plaque composition may provide valuable information on the risk for rupture (Saba *et al* 2014). Atherosclerotic plaques can be divided into two categories based on their morphology and composition: vulnerable and stable plaques (Finn *et al* 2010). Vulnerable plaques are characterized by the presence of a large lipid core, covered by a thin fibrous cap and increased macrophages. It has also been demonstrated that plaque inflammation promotes the development of vulnerable features and increases the risk for rupture (Finn *et al* 2010, Drakopoulou *et al* 2011). These characteristics have been reported to be associated with lower stiffness (Czernuszewicz *et al* 2015). On the other hand, stiffening of the plaque's necrotic core due to calcification, or the presence of a thick fibrous cap consisting of smooth muscle cells in an extracellular matrix rich in type I and III collagen, are characteristics that have been reported to contribute to the stability of the plaque (Nandalur *et al* 2007, Nadkarni *et al* 2009, Drakopoulou *et al* 2011).

Ultrasound imaging has shown great promise as a low cost, non-invasive tool to provide information on plaque composition. Several techniques have focused on quantitative intensity analysis of ultrasound images (Grønholdt *et al* 1998, Golemati *et al* 2013a, 2013b, 2014, Huang *et al* 2016b, Mitchell *et al* 2017). The rationale is that softer plaques, characterized by high lipid content or hemorrhage, are expected to generate weak reflections of ultrasound waves. On the other hand, calcifications appear as echo-rich regions that cause acoustic shadowing. Even though such methods have shown promise in vulnerable plaque identification, there is still the need to develop a tool that provides mechanical characterization of atherosclerotic plaques (de Korte *et al* 2016).

Ultrasound Elastography methods have been utilized for arterial wall and plaque stiffness estimation. Such methods involve acquisition of ultrasound image sequences, and then calculation of the imaged tissue's deformation and strain, usually by applying cross correlation on the RF signals and performing spatial displacement differentiation. Imaging blood pressure induced strain in atherosclerotic lesions has shown promise in detecting vulnerable plaques (Hansen *et al* 2013, de Korte *et al* 2016, Hansen *et al* 2016, Roy Cardinal *et al* 2017, Dempsey *et al* 2018). Acoustic radiation force imaging (ARFI) employs acoustic radiation force to displace the tissue under study, and then measure the resulting deformation. Application of this technique in 4 pre-operative carotid artery disease patients and comparison with histology, demonstrated the feasibility to differentiate between stable and unstable plaque components based on the measured displacements (Czernuszewicz *et al* 2015). Shear wave elastography (SWE), which estimates plaque elasticity by tracking the ARFI induced shear wave propagation, has also been shown capable of plaque vulnerability assessment (Ramnarine *et al* 2014, Garrard *et al* 2015, Widman *et al* 2015).

Pulse wave velocity (PWV) is a cardiovascular parameter that is linked to arterial stiffness and has been associated with cardiovascular morbidity and mortality (van Popele *et al* 2001, Laurent *et al* 2006). Pulse wave imaging (PWI) (Fujikura *et al* 2007, Li *et al* 2013, Nandlall *et al* 2014, Apostolakis *et al* 2017b, Nauleau *et al* 2018) is a non-invasive ultrasound-based method which tracks the propagation of the distension pulse wave (PW) along an arterial segment, enabling estimation of regional PWV. In turn, PWV can be associated, under specific assumptions, to the Young's modulus and compliance of the imaged vessel, through the Moens–Korteweg and Bramwell–Hill equations, respectively. PWI, combined with arterial wall strain imaging, has been shown to be capable of differentiating among plaques with different degrees of calcification (Li *et al* 2018). Alternative ultrasound methods for non-invasive determination of PWV have also been developed by several other groups (Borlotti *et al* 2012, Hasegawa *et al* 2013, Kruizinga *et al* 2014, Negoita *et al* 2017).

PWI was previously extended by developing piecewise PWI (pPWI), which provides sub-regional piecewise PWV estimation by sliding a kernel with a fixed size of a few millimeters along the imaged arterial segment (Apostolakis *et al* 2016). However, in the case of atherosclerotic arteries, spatial variation in arterial wall mechanical properties may affect the pulse wave propagation, reducing thus the reliability of stiffness calculation. Pulse wave reflections generated at wall inhomogeneity points, as well as the transition between inhomogeneous segments, bias the PWV and piecewise PWV estimation (Li *et al* 2018).

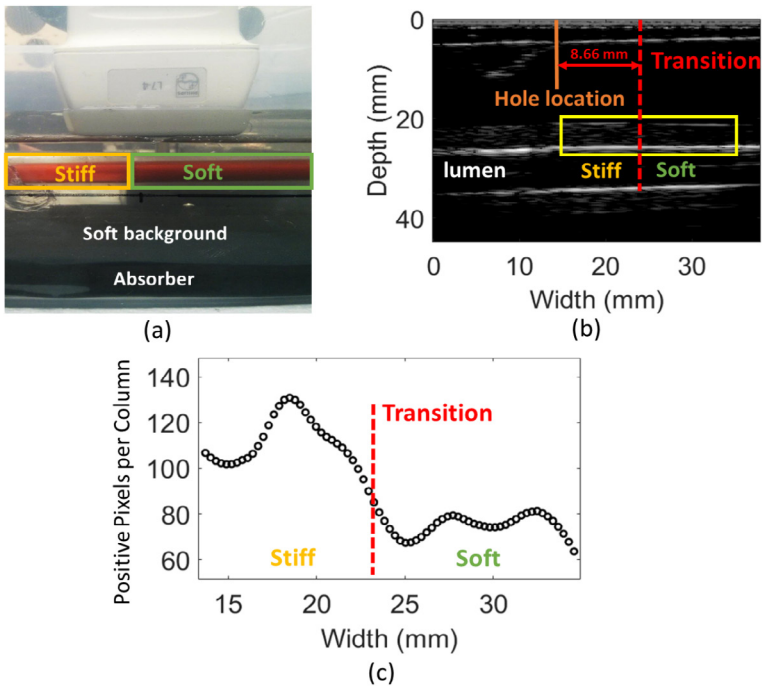

Figure 1. (a) Phantom experimental setup. (b) Acquired B-mode image of a longitudinal view of the phantom. The yellow rectangle illustrates the segment of the anterior wall which was selected to identify the stiffness transition. (c) Function of positive pixels per column (ppc(x)), which quantifies ultrasound scatterer concentration with respect to the lateral position in the selected region of the anterior phantom wall.

To address those challenges, adaptive PWI was introduced, which identifies spatial variations in arterial wall properties across the imaged vessel (Apostolakis 2018, Apostolakis *et al* 2019). Instead of using a kernel of fixed size as in the case of pPWI, adaptive PWI uses a dynamic programming technique over a graph modeling framework, in order to determine the arterial segments where the PW propagation is most homogeneous, based on the spatiotemporal variation of the arterial wall distension. Thus, the artery is divided into the segments with most homogeneous properties, and a more robust piecewise PWV estimate is provided for each one of those segments. Adaptive PWI demonstrated the potential to detect early stages of atherosclerosis in murine aortas *in vivo* by capturing the progression of the level of arterial wall inhomogeneity and change in vessel wall stiffness due to arterial wall remodeling. Moreover, the proposed method was capable of delineating the extent of abdominal aortic aneurisms in murine aortas, while initial feasibility was shown to detect vessel wall abnormalities in three atherosclerotic human carotid arteries. However, the capability of adaptive PWI to provide atherosclerotic plaque mechanical characterization and plaque vulnerability assessment, or to evaluate the effect of age-induced vascular wall degeneration in arterial wall properties has not been investigated. Furthermore, interference of pulse wave reflections generated at transitions in vessel wall stiffness and geometry degraded the accuracy of inhomogeneity detection and wall characterization.

In the present study an improved version of adaptive PWI was developed, which employs more robust markers based on the spatiotemporal variation of the arterial wall distension for wall inhomogeneity identification and regional stiffness characterization. The presented method was evaluated against the previous adaptive PWI implementation, in the same phantom experimental setup, providing smaller errors both in inhomogeneity detection and PWV estimation. Furthermore, adaptive PWI was tested in the carotid arteries of non-atherosclerotic subjects in different age groups, as well as in atherosclerotic arteries which are expected to present more irregular properties. Application of the proposed algorithm *in vivo* demonstrated its capability to capture changes in vessel wall homogeneity and/or arterial compliance associated with ageing and carotid artery disease. Finally, adaptive PWI showed the feasibility to provide a surrogate estimate of plaque stiffness, which was capable of differentiating between calcified and non-calcified or high lipid plaques.

2. Methods

2.1. Phantom study

The experimental setup presented in Nauleau *et al* (2018) was employed in this study (figure 1(a)), in order to compare the wall inhomogeneity detection and mechanical characterization capability of the proposed algorithm, against the previous adaptive PWI implementation (Apostolakis 2018, Apostolakis *et al* 2019). A

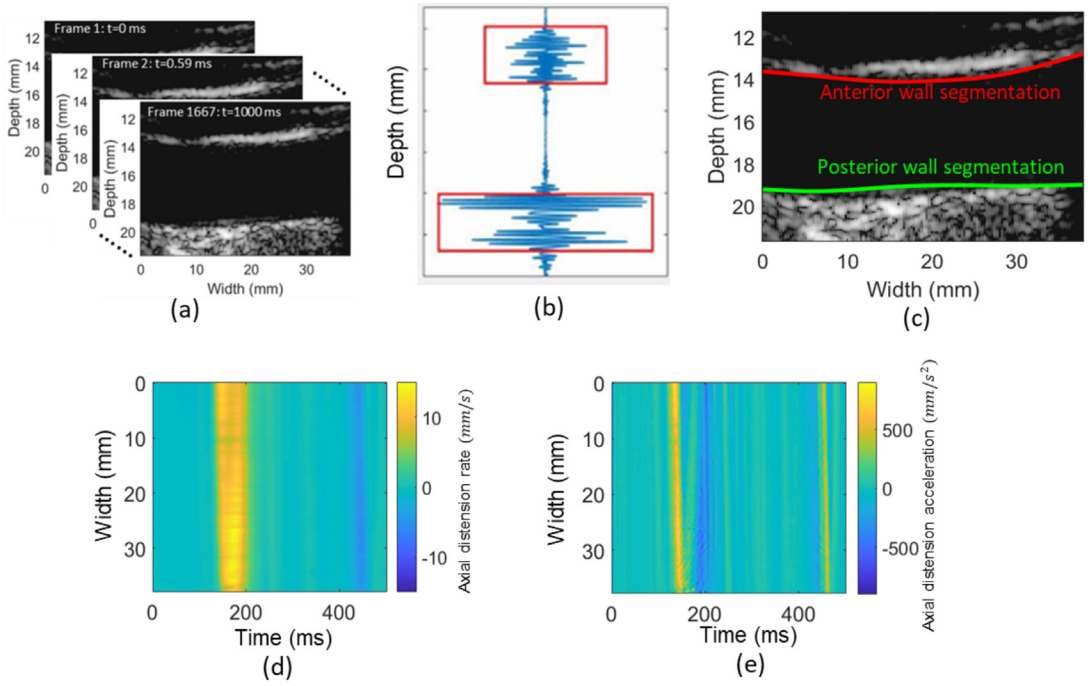

Figure 2. PWI methodology: (a) RF frames are acquired from a longitudinal view of the carotid artery at a high frame rate. (b) A 1D cross correlation method is applied on the RF data for axial inter-frame displacement estimation. (c) Manual segmentation of anterior and posterior arterial walls. (d) Spatiotemporal plot of axial distension rate. (e) Spatiotemporal plot of axial distension acceleration obtained through temporal differentiation of axial distension rate.

silicone phantom consisting of a soft and stiff segment along the longitudinal axis, embedded in soft surrounding material was employed, with the stiff phantom segment containing higher concentration of ultrasound scatterers. The PWV values of both segments were estimated through static testing (Nauleau *et al* 2018). Pulses were generated by releasing a pinch inside the phantom. A small hole was made on the top surface of the surrounding material, which was used as a marker to locate the stiff/soft interface.

In addition, an analysis was performed on the acquired B-mode images ($N = 8$), in order to track the stiffness transition based on the different scatterer concentration used for the construction of the two phantom segments (Apostolakis *et al* 2019). In each B-mode a 20 mm region of the phantom anterior wall was selected, which was known to include the transition, by using the hole as a reference (figure 1(b)). The pixels of the selected region were thresholded, with a threshold of 20% the brightness range, obtaining thus a binary image. The pixels with a value of 1 were summed along each column of the binary image, obtaining thus the function of positive pixels per column (ppc(x)), which quantifies the ultrasound scatterer concentration with respect to the lateral position. The resulting function was then smoothed using a second order Savitzky–Golay filter with a Kernel of 13 points (figure 1(c)). The transition from the stiff to the soft segment was defined as the lateral position where the spatial derivative of ppc(x) is minimum, and was found to be 8.66 ± 0.58 mm ($N = 8$) away from the hole.

2.2. *In vivo* study

The common carotid arteries of $N = 9$ young subjects (9 Male, 22–32 y.o.) and $N = 9$ elderly subjects (6 Male, 3 Female, 60–73 y.o.) with no prior history of carotid artery disease were scanned, *in vivo*. The age was significantly lower in the young, compared to the older group as assessed through unpaired t-test (26.11 ± 2.8 y.o. versus 64.67 ± 4.85 y.o., p-value < 0.0001). Additionally, the atherosclerotic carotid arteries of $N = 12$ (6 Female, 6 Male 59–85 y.o.) diagnosed with carotid artery disease were scanned at the plaque site, with $N = 3$ presenting low (<50%), $N = 5$ moderate (>50%) and $N = 4$ high (>80%) degree of stenosis. Unpaired t-test indicated that there was not significant difference in ages between non-atherosclerotic elderly group and carotid artery disease patients (64.67 ± 4.85 y.o versus 70.58 ± 8.40 y.o., p-value > 0.05). Carotid artery disease patients were recruited at the neurological institute of Columbia university medical center while they were undergoing inpatient care, or before they get admitted for carotid endarterectomy. Screening and recruitment of carotid artery disease subjects was performed in collaboration with the patients' examining or treating physicians. All procedures performed for the human study were approved by the Human Research Protection Office (HRPO) and Institutional Review Boards (IRBs) of Columbia University (Protocol no. AAAR0022).

The carotid artery disease patients were divided into two groups based on the composition of the imaged atherosclerotic plaque. Group 1 ($N = 5$) included calcified, or severely calcified plaques, which are characterized

Table 1. Patient characteristics.

Patient	Sex	Age	Stenosis	Calcified	Assessment method
Patient 1	F	73	High	Yes	H[a]
Patient 2	F	72	Moderate	Yes	H
Patient 3	F	77	High	No	H
Patient 4	F	85	Low	No	H
Patient 5	F	73	High	Yes	H
Patient 6	M	61	Moderate	No	G. P.[b]
Patient 7	M	81	High	Yes	G. P.
Patient 8	M	75	Moderate	No	G. P.
Patient 9	F	62	Moderate	No	G. P.
Patient 10	M	59	Low	No	MRI & CT neck
Patient 11	M	67	Moderate	Yes	CT neck
Patient 12	M	62	Low	No	CT neck

[a] H: Histology.
[b] GP: Gross pathology.

by increased stiffness. Group 2 ($N = 7$) consists of patients with non-calcified and/or high lipid plaques. Nine of the patients included in the study underwent carotid endarterectomy and were assigned to one of the two groups based on gross pathology evaluation, made by the operating surgeon. In five out of nine patients, a plaque sample was retrieved and histological examination was performed by an expert pathologist. In those cases, plaque categorization was made based on histological examination. Four of the plaque samples were stained along the artery's longitudinal axis, and the boundaries of the atherosclerotic lesions were determined as the start of intima thickening at the shoulders of the plaque. The average length of the four atherosclerotic lesions was 11.21 ± 3.74 mm. In the remaining three patients, MRI and/or CT neck scans were available and their plaque was classified based on the clinical diagnosis. Nine out of twelve carotid artery disease patients were on statin therapy. Table 1 summarizes patient information such as age, gender, degree of stenosis, type of plaque, and the method used for plaque classification.

2.3. Acquisition setup

A Verasonics Vantage 256 system (Verasonics, Kirkland, USA) was used to drive an L7-4 linear array transducer with 128 elements, at a center frequency of 5 MHz and 50% bandwidth. A coherent compounding sequence involving the transmission of 3, 5, or 9 plane waves was implemented at a pulse repetition frequency of 8333 Hz (Apostolakis *et al* 2017a). The RF sampling rate was at 20 MHz. In the case of the phantom experiment, the phantom was imaged longitudinally at the soft/stiff segment interface. Two sets of 4 acquisitions were performed as in Apostolakis *et al* (2019), with the pulse wave propagating from the soft to stiff segment, and the stiff to soft segment, respectively. In the *in vivo* study, longitudinal images of the common carotid were acquired, up to the level of carotid bifurcation.

2.4. PWI processing

A similar methodology as in Apostolakis *et al* (2017b) was performed (figure 2). The acquired RF data were beamformed by using the delay and sum algorithm implemented in CUDA. A GPU-accelerated, parallelized version of the sum-table 1D normalized cross-correlation method was applied on the acquired RF signals in order to estimate the axial inter-frame displacements, and then normalized with the frame rate to obtain the axial velocities. The anterior and posterior arterial walls were then manually segmented, and the temporal waveform of the axial distension rate of each wall ($v_{i,\text{anterior}}(t)$ and $v_{i,\text{posterior}}(t)$, respectively) were obtained at each lateral position i, $i = 1,2,\ldots,128$, along the imaged arterial segment. In order to eliminate possible rigid motion, $v_{i,\text{posterior}}(t)$ was subtracted from $v_{i,\text{anterior}}(t)$. Thus, a spatiotemporal map of the axial distension rate ($v_i(t) = v_{i,\text{anterior}}(t) - v_{i,\text{posterior}}(t)$) was generated, which has shown to provide more robust pulse wave (PW) tracking (Huang *et al* 2016a). Subsequently, a median filter using a 3×3 kernel was applied on the spatiotemporal map of the axial distension rate ($v_i(t)$), and differentiation in the time domain was performed in order to obtain the temporal waveform of the axial distension acceleration ($\alpha_i(t) = \mathrm{d}v_i(t)/\mathrm{d}t$) at each lateral position.

2.5. Spatial mechanical inhomogeneity detection

In the previous adaptive PWI implementation, vessel wall homogeneity was evaluated based on the linearity of pulse wave propagation using the axial distension rate waveforms ($v_i(t)$), and the homogeneity of peak axial distension rate ($v_{i,\text{peak}}$) (Apostolakis 2018, Apostolakis *et al* 2019). In this study, the following two criteria are used:

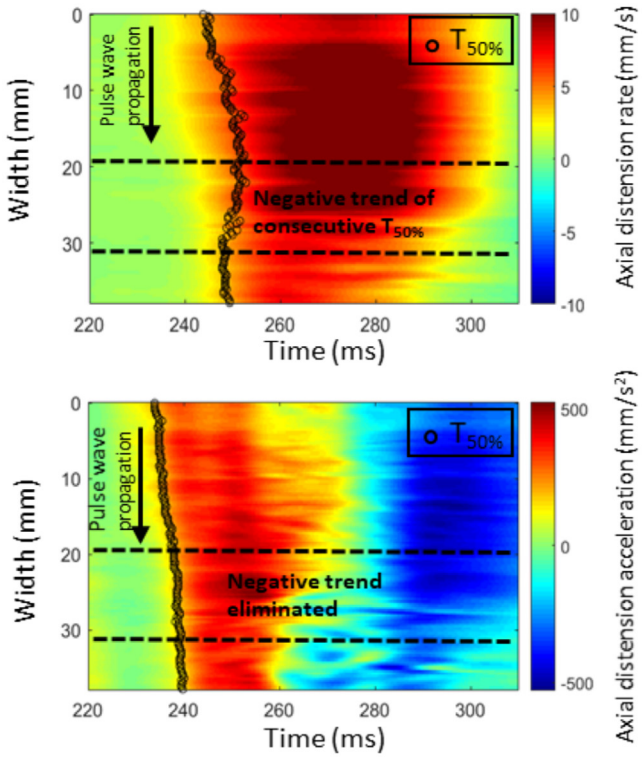

Figure 3. Spatiotemporal plots with 50% upstroke markers of (a) axial distension rate ($v_i(t)$) and (b) axial distension acceleration ($\alpha_i(t)$), obtained through temporal differentiation of $v_i(t)$. Both plots are obtained from the same acquisition in an atherosclerotic carotid artery *in vivo*.

- the area under the curve (AUC_i) of the cross-correlation function between the axial distension rate waveform at the first lateral position ($v_1(t)$) and each one of the subsequent lateral positions ($v_i(t), i = 2,3,\ldots,128$) (Nauleau *et al* 2018).
- linearity of PW propagation based on the axial distension acceleration waveforms ($\alpha_i(t) = \mathrm{d}v_i(t)/\mathrm{d}t$)

AUC_i is an index of similarity among displacement waveforms at different lateral positions and has demonstrated the feasibility to identify transitions in arterial wall mechanical properties. This marker was chosen over $v_{i,\mathrm{peak}}$, because it evaluates the arterial wall homogeneity based on the entire $v_i(t)$ waveform, instead of a single peak point, and is thus expected to be less affected by noise and provide more robust inhomogeneity detection (Laurent *et al* 2006).

In the case of the human study, the linearity of PW propagation was evaluated by tracking the 50% upstroke time point ($T_{50\%,i}$) of the axial distension acceleration waveform at each lateral position, i. In the case of the phantom study, due to the low degree of distension generated by the pinch release method, the $v_i(t)$ waveform is more susceptible to electronic noise (Bunting *et al* 2014, Apostolakis *et al* 2017a). This effect is also present in the axial distension acceleration waveform, resulting in noisy $T_{50\%,i}$. Thus, we chose to track the PW propagation at the steepest transition of $v_i(t)$, which corresponds to the most prominent peak of the axial distension acceleration waveform $\alpha_i(t)$ ($T_{\mathrm{peak},i}$), and was found to be less affected by noise. The acceleration was selected to evaluate the linearity of PW propagation, because it amplifies higher frequency components, providing thus better temporal resolution in calculating the time shift of the waveform among different lateral positions due to the PW propagation (Hasegawa *et al* 2013, Nagaoka *et al* 2015). In a previous study involving application of PWI in atherosclerosis patients, negative piecewise PWV values were reported by tracking the 50% upstroke in the $v_i(t)$ spatiotemporal map, and this was attributed to the effect of pulse wave reflections, travelling in the opposite direction and merging with the forward main wave (Li *et al* 2018). Figure 3(a) illustrates an example of this effect in an atherosclerotic carotid artery *in vivo*, where the 50% upstroke points $v_i(t)$ appear to follow a negative trend in the marked region. Figure 3(b) demonstrates the corresponding axial distension acceleration spatiotemporal map as obtained through temporal differentiation of $v_i(t)$. We can observe that the acceleration spatiotemporal plot provides more accurate tracking of the forward wave, alleviating the appearance of negative PW propagation. This is in agreement with another study (Nagaoka *et al* 2015), where the acceleration waveform was found to provide better seperation of the forward and reflected pulse wave in time.

Subsequently, an outlier correction process was performed in order to prevent our algorithm from erroneously identifying noisy $T_{50\%}$ points as wall inhomogeneity points. A robust linear fit was applied on the

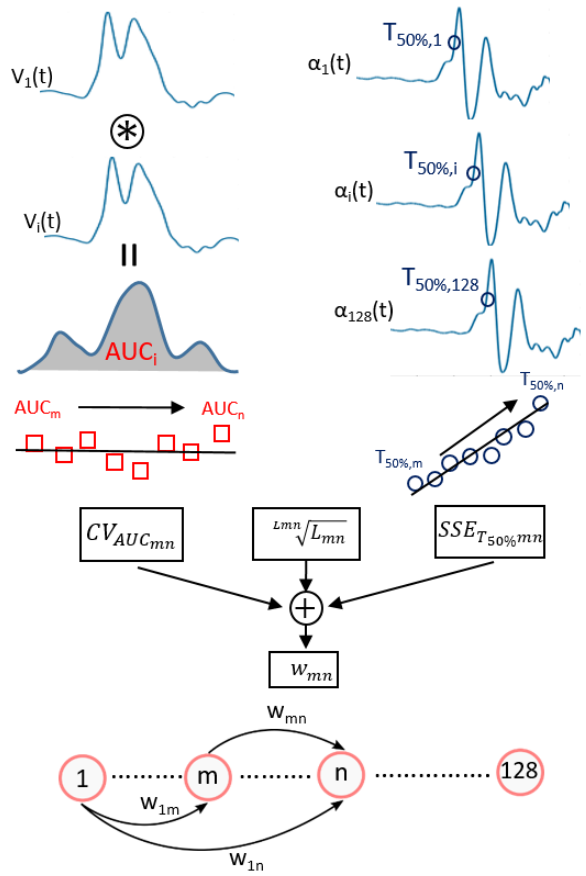

Figure 4. Calculation AUC_i and $T_{50\%,i}$ to evaluate the similarity of $v_i(t)$ waveforms among different lateral positions and linearity of PW propagation, respectively. Weight calculation and graph modelling approach to identify the individual arterial segments, where the pulse wave propagation is most uniform. The illustrated $v_i(t)$ and $\alpha_i(t)$ waveforms are obtained by a young healthy subject.

consecutive $T_{50\%,i}$, across the entire imaging width (i.e. for $i = 1$ to 128). Points whose residual error from the linear fit was higher than 5 times the median residual error of all points were considered as outliers and were placed onto the fitted line.

A similar graph modelling approach as in Apostolakis (2018) and Apostolakis *et al* (2019) was employed to determine the longitudinal arterial segments that yield the most uniform AUC_i values and most Linear $T_{50\%,i}$ points (figure 4). A graph was formed with each graph node representing a lateral position, and each node connected to subsequent nodes through graph edges. Each graph edge connecting two nodes $m, n, m > n$ was linked to a weight (w_{mn}), which represents the homogeneity of pulse wave propagation from lateral position m to n:

$$W_{mn} = \mathrm{SSE}_{T_{50\%}mn} + \mathrm{CV}_{\mathrm{AUC}mn} + \sqrt[L_{mn}]{L_{mn}}. \quad (1)$$

Where $\mathrm{SSE}_{T50\%mn}$ denotes the sum of squared errors of linear fit to consecutive $T_{50\%,i}$ and $\mathrm{CV}_{\mathrm{AUC}mn}$ the coefficient of variation of consecutive AUC_i, for i between m and n. $\sqrt[L_{mn}]{L_{mn}}$ is a penalty involving the length of the detected homogeneous segments. We used $\sqrt[x]{x}$, a function which rises sharply from $x = 0$ to $x = e$ and then slowly decreases. This function was scaled so that it reaches its maximum for approximately half the length of the field of view. The three metrics were normalized to receive their minimum and maximum value at 0 and 1, respectively. The individual segments with most homogeneous pulse wave propagation were considered to be the segments corresponding to the path, i.e. the collection of graph edges, that connect the first and last node and yield minimum average w_{mn}. By treating the sum of w_{mn} as the total path distance, the edges that minimize w_{mn} were identified by applying the shortest-paths Bellman–Ford algorithm. The nodes that connect the edges of the determined shortest path, represent the lateral positions corresponding to the interfaces of the most homogeneous segments.

2.6. Arterial wall characterization

Let N be the number of homogeneous segments in which the artery is divided by adaptive PWI, and $m_1, m_2, \ldots, m_{N-1}$ denote the lateral positions of the interfaces between consecutive homogeneous segments. For each segment k∈[1 N], piecewise arterial wall characterization was performed by estimating PWV and Compliance:

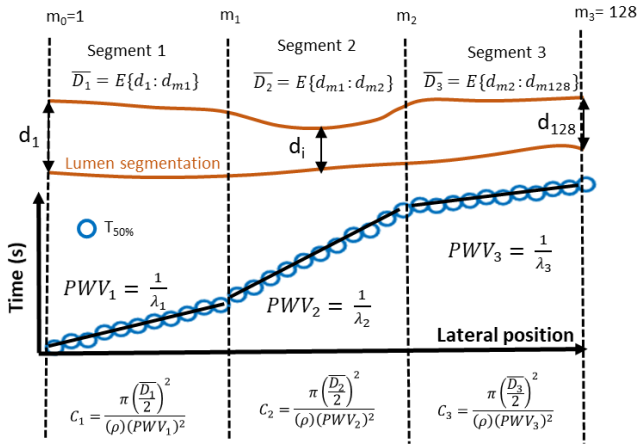

Figure 5. Diameter and PWV calculation, for piecewise arterial wall Compliance estimation through the Bramwell–Hill model.

- **Pulse wave velocity (PWV_k):** PWV_k in each segment k was calculated as the inverse of the slope of a linear fit applied to consecutive $T_{50\%,i}$ (or $T_{peak,i}$ in the case of the phantom study) (expressed in s) versus the lateral position i (expressed in m), for $i \in [m_{k-1}\ m_k]$.
- **Compliance (C_k):** The arterial lumen was manually segmented by an expert sonographer, and two smooth lines were generated depicting the interface between the arterial walls and the lumen. The axial distension rate values ($v_i(t)$) were also used to move the lines accordingly. Thus, by subtracting the axial position of the posterior wall line from the anterior wall line, the time waveform of the luminal diameter $d_i(t)$ at each lateral position, i, was obtained. Since the pulse wave is tracked at the systolic foot of the pulse, we only considered the diameter d_i at the time frame where $d_i(t)$ was minimum. In each homogeneous segment k, the average diameter was calculated as $\overline{D_k} = E\{d_i\}$, for $i \in [m_{k-1}\ m_k]$, and a piecewise Compliance value was obtained through the Bramwell–Hill equation:

$$C_k = \frac{\pi\left(\frac{\overline{D_k}}{2}\right)^2}{(\rho)\,(\mathrm{PWV}_k)^2} \tag{2}$$

where $E\{\}$ denotes the averaging operator, and ρ is the density of blood assumed to be equal to 1060 kg m^{-3}. Figure 5 illustrates the methodology for piecewise compliance estimation for a number of homogeneous segments $N = 3$.

In the case of non-atherosclerotic carotid arteries, a single average compliance value was obtained by calculating the mean piecewise compliance of the detected homogeneous segments. In the case of atherosclerotic subjects, the average compliance of the stenotic segment was calculated. The stenotic segment was defined by employing an independently developed algorithm for plaque detection, using the diameter measurements obtained through manual wall segmentation. In short, the lateral position, i_{min}, corresponding to the minimum diameter ($\min\{d_i\}$) is calculated. The lateral position preceding i_{min}, where the second derivative of the diameter reaches its minimum ($\min\{d^2(d_i)/di^2\}$) is defined as the left boundary of the plaque (left blue solid line). The lateral position following i_{min}, where the second derivative of the diameter reaches its maximum ($\max\{d^2(d_i)/di^2\}$) is defined as the plaque's right boundary. In one patient where the entire plaque was in the field of view, the length of the stenotic segment obtained through adaptive PWI was compared with the length of the plaque determined through histological examination.

One-way ANOVA with Holm–Sidak correction was carried out to compare the piecewise compliance estimated for the stenotic segment in patients with calficied plaques, non-calcified/high lipid plaques, and average piecewise compliance in elderly non-atherosclerotic subjects. The same statistical test was also performed to assess differences in the number of detected homogeneous segments among atherosclerotic subjects, non-atherosclerotic elderly subjects and young subjects. Comparison of the average piecewise compliance was carried out between non atherosclerotic young and elderly subjects, by using unpaired t-test.

3. Results

3.1. Phantom study

Figure 6 illustrates the inhomogeneity detection capabilities of the proposed algorithm in the phantom experiment. The yellow dashed lines illustrate the boundaries of the most homogeneous segments identified

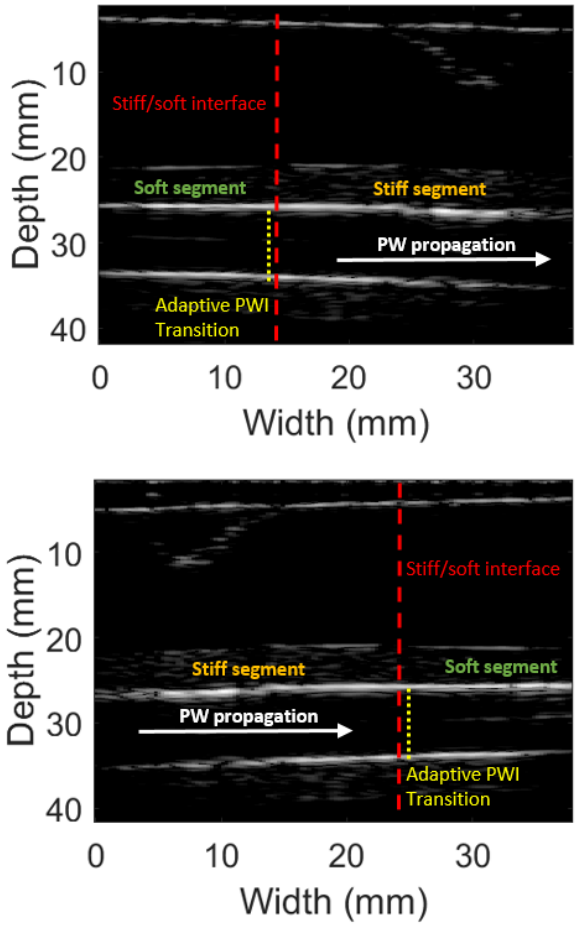

Figure 6. Inhomogeneity detection in a silicone phantom consisting of a soft and a stiff segment. Top and bottom figures illustrate the detected stiff/soft interface for the pulse wave propagating from the soft to stiff and stiff to soft direction, respectively.

Table 2. Summary of phantom experiment results.

	AUC$_i$ & $\alpha_i(t)$ tracking		$V_{i,\text{peak}}$ & $v_i(t)$ tracking (Apostolakis *et al* 2019)		
	Soft-stiff ($N = 4$)	Stiff-soft ($N = 4$)	Soft-stiff ($N = 4$)	Stiff-soft ($N = 4$)	Static
PWVsoft (m s^{-1})	2.47 ± 0.04	2.60 ± 0.18	2.34 ± 0.09	2.93 ± 0.08	2.41
PWVstiff (m s^{-1})	3.43 ± 0.08	3.72 ± 0.08	3.59 ± 0.06	3.96 ± 0.28	3.52
Transition error (mm)	0.98 ± 0.49	1.04 ± 0.27	3.64 ± 0.14	4.67 ± 0.73	—

by the adaptive PWI. The red dashed line shows the position of the mechanical transition from the soft to the stiff segment of the phantom. The proposed algorithm provided good approximation of the stiffness transition location, with an error of 0.98 ± 0.49 mm in the case of pulse wave propagation from the soft to the stiff phantom segment, and 1.04 ± 0.27 mm for the stiff to soft propagation direction. Moreover, piecewise PWVs were in good agreement with static testing for both directions of pulse wave propagation. Table 2 summarizes the errors in transition detection and PWVs of the proposed algorithm (AUC$_i$ & $\alpha_i(t)$ tracking), in comparison with the previous adaptive PWI implementation ($v_{i,\text{peak}}$ & $v_i(t)$ tracking) (Apostolakis *et al* 2019), which employed the peak values and peak time points of the axial distension rate as markers of vessel wall homogeneity. We can observe that using AUC$_i$ and tracking the PW through the axial distension acceleration waveform provided smaller errors of mechanical property transition detection.

3.2. *In vivo* study

Figures 7(a) and (b) illustrates the output of the proposed algorithm in two young subjects (F and M, 26 and 22 y.o., respectively), and (c) in a non-atherosclerotic subject in the elderly group (M, 68 y.o.). The yellow dashed lines indicate the boundaries of homogeneous segments provided by adaptive PWI, while the estimated arterial Compliance was color-coded and overlaid onto the B-mode. We can observe that in all three cases, the algorithm generated a single homogeneous segment along the imaged artery, indicating homogeneous PW propagation.

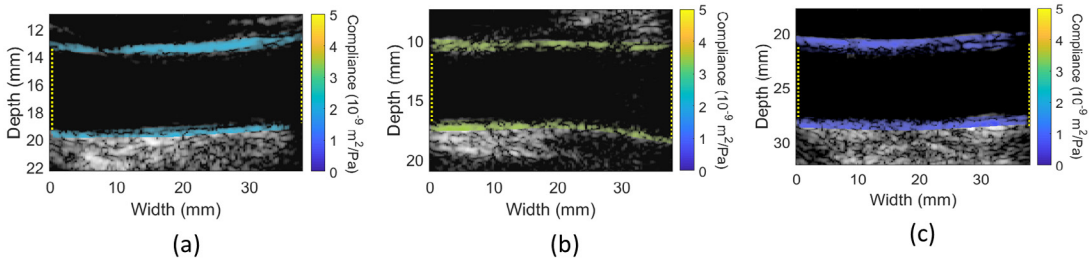

Figure 7. Output of adaptive PWI, with the estimated arterial Compliance color-coded and overlaid onto the B-mode in (a) and (b) 2 healthy young subjects (F and M, 26 and 22 y.o., respectively), and (c) in a non-atherosclerotic subject in the elderly group (M, 68 y.o.).

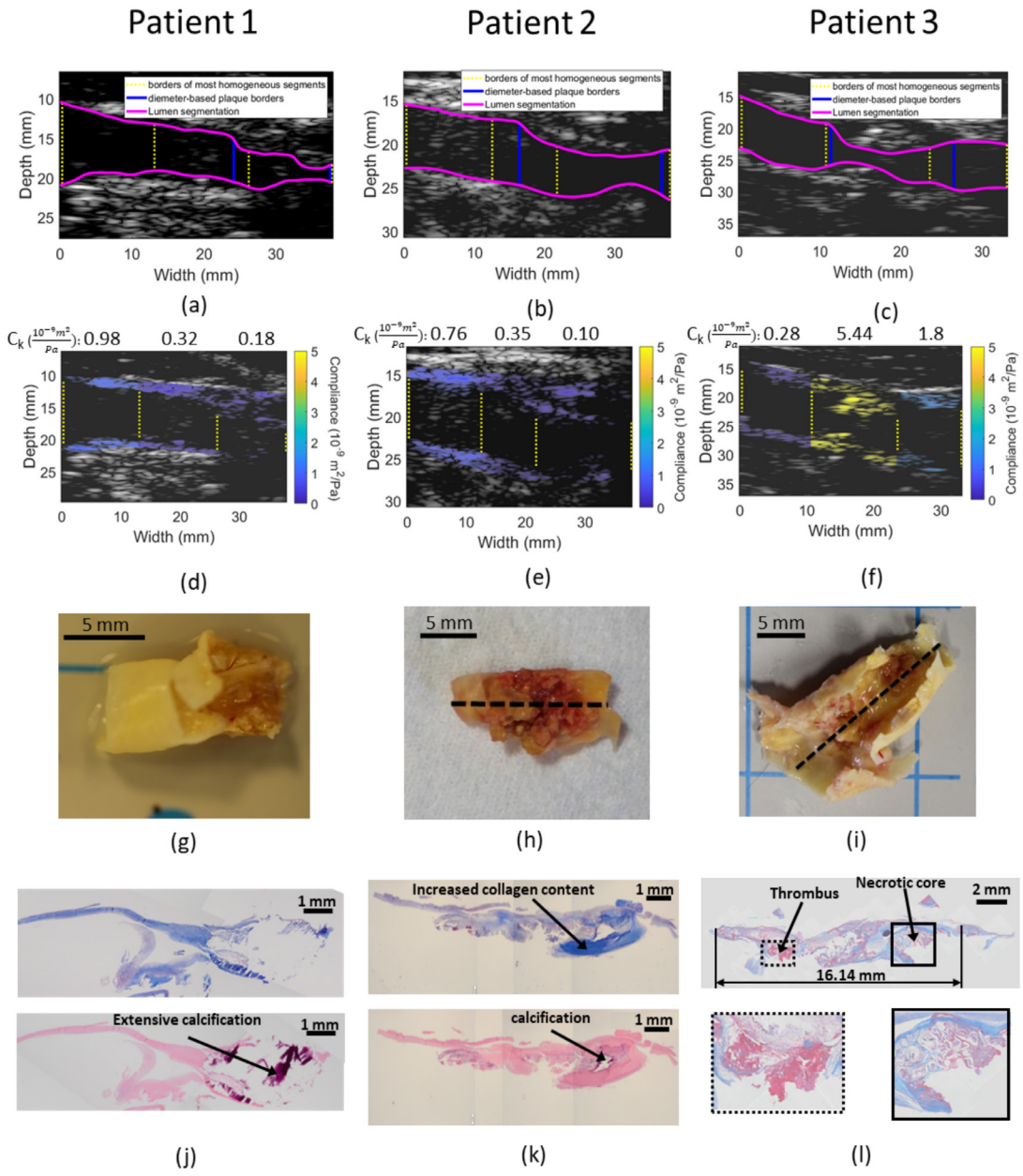

Figure 8. Examples of 3 carotid artery disease, whose plaque sampled where retrieved and sent for histology. Each column refers to a different patient. (a)–(c) illustrate the boundaries of the most homogeneous segments detected by the adaptive PWI in yellow dashed lines in the corresponding patient. Magenta lines illustrate the extent of the anterior and posterior walls, as obtained through manual segmentation. The blue solid lines demonstrate the output of an independently developed algorithm for plaque detection based on lumen diameter measurements. (d)–(f) show compliance in each most homogeneous segment, color-coded and overlaid onto the B-mode image. (g)– (i) demonstrate the plaque sample obtained in each patient after carotid endarterectomy, while (j)–(l) show a histological slice obtained through H&E and Masson's Trichrome.

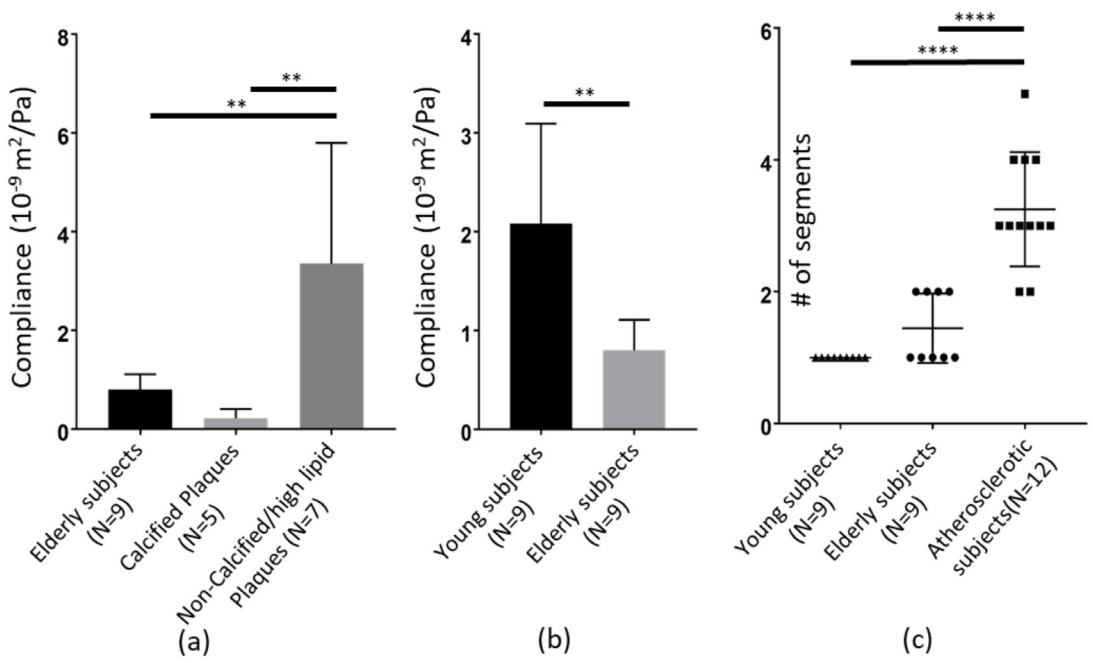

Figure 9. (a) Mean and standard deviation of arterial compliance estimated by adaptive PWI in elderly subjects, stenotic segment in calcified plaques, and stenotic segment in non-calcified/high-lipid plaques. (b) Mean and standard deviation of arterial compliance estimated by adaptive PWI in elderly and young subjects. (c) Number of individual homogeneous segments in which the artery was divided in young, elderly and atherosclerotic subjects.

Moreover, lower compliance was calculated for the elderly non-atherosclerotic subject ($0.73 * 10^{-9}$m^2 Pa^{-1}) compared to young ones ($2.1 * 10^{-9}$ and $3.75 * 10^{-9}$m^2 Pa^{-1}).

Figure 8 illustrates three examples of carotid artery disease patients who underwent carotid endarterectomy and their plaque samples underwent histological examination. Figures 8(a)–(c) show the boundaries of the most homogeneous segments detected by the adaptive PWI in yellow dashed lines. Magenta lines illustrate the extent of the anterior and posterior walls, as obtained through manual segmentation, in order to calculate the lumen diameter (described in Section II-F). The blue solid lines demonstrate the boundaries of the stenotic segment, as determined through lumen manual segmentation, using the method described in section II-E. In each patient, the segments of the adaptive PWI corresponding to the stenotic segment were defined as those segments, whose boundaries are closest to the blue solid lines. Figures 8(d)–(f) illustrate the compliance estimated in each most homogeneous segment, color-coded and overlaid onto the B-mode image. Moreover, the compliance value calculated for each segment is written on the top of the corresponding image. Figures 8(g)–(i) illustrate the plaque sample obtained after carotid endarterectomy, while (j)– (l) demonstrate the H&E and Masson's trichrome staining of a histological slice.

Adaptive PWI provided three segments for those three patients, indicating increased vessel wall inhomogeneity. In patient 1, a low compliance estimate was produced for the stenotic segment, which is in agreement with the histology sample, demonstrating severe calcification, which increases the plaque stiffness and contributes to its stability. We can also observe a low compliance in the case of patient 2, in coherence with histological examination, which showed calcification and higher collagen content (blue color in Masson's trichrome test), components that are also linked with increased stiffness. In patient 3, adaptive PWI identified a stenotic segment with high compliance value, as compared to healthy subjects and patients with calcified plaques. This was corroborated with H&E and Masson's trichrome findings, which revealed a plaque with a large necrotic core and the presence of a thrombus. Those characteristics are associated with reduced stiffness and are signs of highly vulnerable plaque. In the case of patient 3, the difference between the plaque length obtained through histological examination (figure 8(l) black double arrow, 16.14 mm) and the length of the stenotic segment obtained through adaptive PWI (13.30 mm) was 2.84 mm.

Figure 9(a) demonstrates that the estimated compliance was significantly higher in the stenotic segment of the non-calcified/high-lipid group, as compared with the stenotic segment of the calcified group ($3.35 \pm 2.45 * 10^{-9}$m^2 Pa^{-1} versus $0.22 \pm 0.18 * 10^{-9}$m^2 Pa^{-1}, p-value < 0.01) and elderly subjects ($3.35 \pm 2.45 * 10^{-9}$m^2 Pa^{-1} versus $0.79 \pm 0.30 * 10^{-9}$m^2 Pa^{-1}, p-value < 0.01). Figure 9(b) illustrates the mean and standard deviation of the compliance estimated by adaptive PWI in young and elderly non-atherosclerotic subjects. Significantly lower compliance was observed in the elderly group, as compared to healthy subjects ($0.79 \pm 0.30 * 10^{-9}$m^2 Pa^{-1} versus $2.08 \pm 1.00 * 10^{-9}$m^2 Pa^{-1}, p-value < 0.01).

Figure 9(c) shows the number of homogeneous segments in which the artery was divided in healthy young, elderly and atherosclerotic subjects. Increased artery fragmentation was observed in the atherosclerotic group as compared to healthy (3.25 ± 0.86 versus 1 ± 0, p-value < 0.0001) and elderly non atherosclerotic subjects (3.25 ± 0.86 versus 1.44 ± 0.51 p-value < 0.0001), indicating increased vessel wall inhomogeneity in atherosclerotic arteries.

4. Discussion

In this study, an enhanced implementation of adaptive PWI was presented, employing more robust markers for arterial wall spatial mechanical inhomogeneity detection and wall characterization. The proposed algorithm was evaluated in a silicone phantom consisting of a stiff and soft segment along its longitudinal axis, and was capable of identifying the transition in mechanical homogeneity and estimating the PWVs of both segments, at a higher accuracy compared to the previous adaptive PWI implementation.

The inhomogeneity detection capability of adaptive PWI was tested *in vivo* by comparing the number of segments generated in the carotid arteries of non-atherosclerotic subjects against atherosclerotic arteries which are expected to present more complex geometry and mechanical properties, affecting thus the homogeneity of pulse wave propagation. Indeed, in carotid artery disease patients, artery fragmentation was found to be significantly higher as compared to non-atherosclerotic young and elderly subjects. A single homogeneous segment was produced in each one of the young subjects, indicating uniform pulse wave propagation and mechanical properties in healthy vessels. In the case of the elderly group, the algorithm produced either one or two segments, suggesting that ageing-induced arterial wall remodelling may have an effect on the homogeneity of wall properties.

Average compliance was significantly lower in elderly non-atherosclerotic subjects as compared to young ones, demonstrating the effect of ageing in arterial wall stiffening. In the case of carotid artery disease patients, arterial wall compliance values provided in the stenotic segment of atherosclerotic arteries demonstrated the feasibility to serve as a surrogate measure of atherosclerotic plaque stiffness, which was capable of differentiating between calcified and non-calcified or high lipid plaques. Comparison with H&E and Masson's trichrome histological examination, showed association between high compliance values, and features associated with plaque vulnerability and reduced plaque stiffness, such as the presence of necrotic core (Hansen *et al* 1995, Mitchell *et al* 2004). Ongoing work focuses on testing this method in a larger cohort of patients to evaluate whether it can provide any additional information to existing ultrasound elastography or B-mode analysis techniques for plaque rupture prediction.

Pulse wave reflections is a phenomenon that limited the performance of the previous adaptive PWI implementation. When the pulse wave travels through a point where the mechanical, or geometrical properties of the vessel change, then a pulse wave reflection is generated that travels in the opposite direction. The reflection coefficient depends on the difference in vascular impedance before and after the transition, which is a function of the vessel's cross-sectional area and stiffness (Borlotti *et al* 2014). This further supports the use of AUC_i as an index to identify mechanical inhomogeneity points, given that the superposition of a reflected wave is expected to change the distension waveform, resulting to different AUC_i values before and after the transition. The axial distension acceleration spatiotemporal map was employed in this study because it is considered to provide more robust pulse wave tracking under the presence of reflections. However, it is still possible that a bias in PWV and compliance estimation is introduced, especially in highly stenotic and calcified plaques, which are expected to have particularly high reflection coefficient.

Adaptive PWI was tested in an idealized case of a phantom with a single transition in vessel wall stiffness. In reality though, atherosclerotic vessels may present more gradual changes in mechanical properties and luminal diameter. In such cases, adaptive PWI should identify the points characterized by the steepest transition in luminal cross sectional area and stiffness which would result in the major change of arterial wall distension pattern. Appendix illustrates the behavior of adaptive PWI in two cases of more gradual transitions, by employing a simplified model of pulse wave propagation. A future step of this work would be to evaluate the accuracy of the proposed method in phantoms and FSI simulated data of atherosclerotic carotid arteries with more realistic wall abnormalities.

The boundaries of most homogeneous segments, were close to, but did not completely match the stenotic segment boundaries identified based on lumen diameter measurements, or the plaque borders obtained through histological examination. Adaptive PWI tracks the lateral positions where the pulse wave and the arterial wall distension waveform change, which do not necessarily coincide with the plaque borders shown in the 2D B-mode images. It is possible that a major change in vessel wall stiffness or cross-sectional area out of the 2D imaging plane influence the pulse wave propagation. Ongoing work includes implementation of this method using 3D PWI (Apostolakis *et al* 2017b), in order to fully investigate mechanical and geometrical inhomogeneity throughout the entire volume of the imaged arterial segment.

A matter that should be investigated is potential bias due to arterial wall segmentation. The Bramwell-Hill model uses the PWV and vessel's cross-sectional area to derive the compliance. In this study though, a 2D longitudinal slice was used to approximate the diameter vessel's cross-sectional area. Moreover, manual wall segmentation can be challenging, especially in cases of calcified plaques, where the presence of acoustic shadowing may obscure the lumen-wall interface. In this study an expert sonographer performed segmentation for lumen diameter measurements, who was blinded to the diagnoses of plaque type. However, employing robust automated wall segmentation algorithms would be a crucial step to support the clinical significance of the proposed method.

Another limitation of this study is that in some patients undergoing carotid endarterectomy, we could not capture the entire length of the plaque. Thus, it was not possible to perform comparison between the stenotic segment obtained by adaptive PWI and plaque length obtained through histological examination in every case. We presented this comparison in one atherosclerotic subject, where the entire plaque could be clearly visualized in the field of view. However, it yet remains to employ robust registration methods between obtained plaque samples and ultrasound scanning site, and test the capability of adaptive PWI to provide the extent of atherosclerotic lesions.

Finally, PWV and arterial wall compliance were estimated by tracking the systolic foot of the pulse wave. However, it has been shown that tracking features corresponding to different points in the cardiac cycle may result in different PWV values (Huang *et al* 2015). This can be justified considering that the stiffness of the arterial wall increases under higher pressure values, due to the engagement of collagen constituents (Vappou *et al* 2010). Future studies will further investigate piecewise compliance variation in atherosclerotic vessels using different pulse wave features during the cardiac cycle.

5. Conclusion

A method was hereby presented that utilizes the PWI information to detect spatial mechanical inhomogeneity across an imaged vessel, and provide piecewise arterial wall compliance estimates. This method was capable of detecting the interface between the soft and stiff segments of a silicone phantom. Furthermore, the feasibility of this method was shown to characterize the arterial wall properties in atherosclerotic carotid arteries *in vivo* which could potentially provide critical information on plaque vulnerability.

Acknowledgments

The authors thank Paul Kemper, MS, Matthias J Szabolcs, MD and Julien Grondin, PhD for their helpful contributions.

This work was supported by a grant of the National Institutes of Health (NIH 1-R01-HL135734)

Appendix. Simulation of gradual transition in vessel wall properties

The simplified 1D model described in Mcgarry *et al* (2016) was employed to simulate the pulse wave propagation in a cylindrical vessel with initial radius, Young's modulus, viscous resistance and length of 4 mm, 32 kPa, 10 s^{-1} and 300 mm, respectively. The inlet boundary condition was a Ricket wavelet pressure waveform, while at the outlet, the flow resistance was fixed at 5×10^{-4} ms^{-1} Pa^{-1}. A more detailed description about this model can be found in Mcgarry *et al* (2016). Adaptive PWI was tested in two different cases: (1) In a case where the vessel's radius reduces gradually up to the point of reaching ¼ of its original value and the arterial wall has uniform stiffness. (2) Same geometry as in case (1) with a transition in the vessel's Young's modulus along the longitudinal axis.

Case 1

Figure A1(a) demonstrates the spatial waveform of the vessel's radius and Young's modulus along the vessel's longitudinal axis. Figure A1(b) shows the corresponding spatial waveforms in a 37.8 mm region including the transition, where adaptive PWI was applied. The width and spatial resolution of the selected region match the size of the field of view in our ultrasound measurements. Figure A1(c) illustrates the spatiotemporal plot of distension rate generated by the model. The black solid lines indicate the borders of most homogeneous segments as determined by adaptive PWI, as well as the PWV values and the R^2 (correlation coefficient) of piecewise linear fits applied to consecutive 50% markers, which indicate the quality of pulse wave tracking. We can observe that adaptive PWI detects the onset of the reduction in vessel's diameter with an error of 1.2 mm. Since the diameter continues to decrease at a constant rate, affecting continuously the linearity of pulse wave propagation, adaptive PWI generates another segment in order to ensure optimal linear fit to 50% upstroke markers and more reliable PWV value.

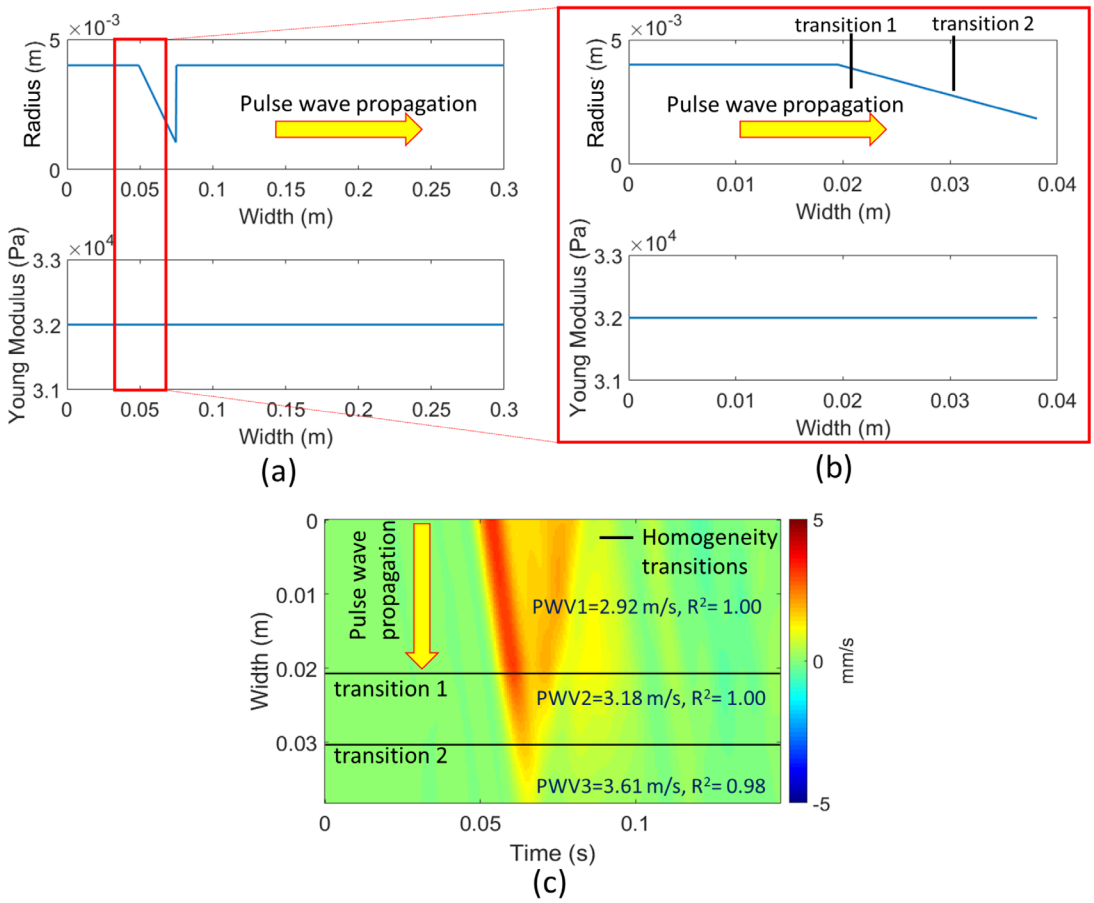

Figure A1. Simulation of vessel with gradual change in radius (a) spatial waveform of the vessel's radius and Young's modulus along the longitudinal axis. (b) Shows the corresponding spatial waveforms in a 37.8 mm region including the transition, where adaptive PWI was applied. The width and spatial resolution of the selected region match the size of the field of view in our ultrasound measurements. (c) Spatiotemporal plot of axial wall distension generated by the model. The black solid lines indicate the borders of most homogeneous segments as determined by adaptive PWI, as well as the PWV values and the R^2 (correlation coefficient) of piecewise linear fits applied to consecutive 50% markers, which indicate the quality of pulse wave tracking.

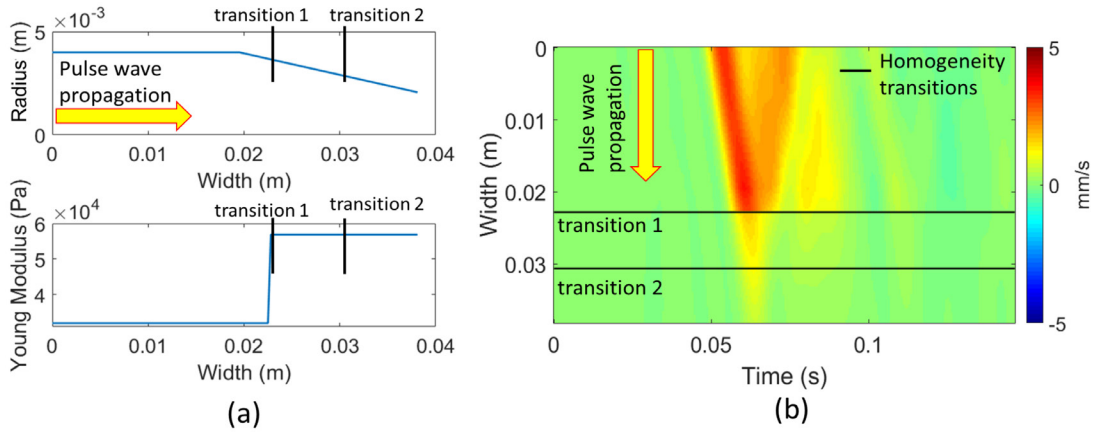

Figure A2. Simulation of vessel with gradual change in radius and transition in Young's modulus.

Case 2

Figure A2(a) shows the spatial waveform of the vessel's radius and Young's modulus. This time, a transition in vessel's Young's modulus occurs 3.3 mm after the point where the radius starts to decrease. Figure A2(b) illustrates the corresponding spatiotemporal plot and adaptive PWI results. In this case, we can observe that adaptive PWI detects the steep stiffness transition, which dominates over the gradual change in vessel's radius, with an accuracy of 0.60 mm. Again, another segment is generated as in case 1, in order to ensure optimal pulse wave tracking.

ORCID iDs

Eliza C Miller https://orcid.org/0000-0002-7108-8906

References

Apostolakis I Z 2018 2D and 3D high frame-rate pulse wave imaging for the characterization of focal vascular disease *Doctoral dissertation* Columbia University

Apostolakis I Z, Karageorgos G M, Nauleau P, Nandlall S D and Konofagou E E 2019 Adaptive pulse wave imaging: automated spatial vessel wall inhomogeneity detection in phantoms and *in vivo IEEE Trans. Med. Imaging* **39** 259–69

Apostolakis I Z, McGarry M D J, Bunting E A and Konofagou E E 2017a Pulse wave imaging using coherent compounding in a phantom and *in vivo Phys. Med. Biol.* **62** 1700–30

Apostolakis I Z, Nandlall S D and Konofagou E E 2016 Piecewise pulse wave imaging (pPWI) for detection and monitoring of focal vascular disease in murine aortas and carotids *in vivo IEEE Trans. Med. Imaging* **35** 13–28

Apostolakis I-Z, Nauleau P, Papadacci C, McGarry M D and Konofagou E E 2017b Feasibility and validation of 4D pulse wave imaging in phantoms and *in vivo IEEE Trans. Ultrason. Ferroelectr. Freq. Control* **64** 1305–17

Borlotti A, Khir A W, Rietzschel E R, De Buyzere M L, Vermeersch S and Segers P 2012 Noninvasive determination of local pulse wave velocity and wave intensity: changes with age and gender in the carotid and femoral arteries of healthy human *J. Appl. Physiol.* **113** 727–35

Borlotti A, Li Y, Parker K H and Khir A W 2014 Experimental evaluation of local wave speed in the presence of reflected waves *J. Biomech.* **47** 87–95

Bunting E A, Provost J and Konofagou E E 2014 Stochastic precision analysis of 2D cardiac strain estimation *in vivo Phys. Med. Biol.* **59** 6841–58

Czernuszewicz T J *et al* 2015 Non-invasive *in vivo* characterization of human carotid plaques with acoustic radiation force impulse ultrasound: comparison with histology after endarterectomy *Ultrasound Med. Biol.* **41** 685–97

de Korte C L, Fekkes S, Nederveen A J, Manniesing R and Hansen H R H G 2016 Review: mechanical characterization of carotid arteries and atherosclerotic plaques *IEEE Trans. Ultrason. Ferroelectr. Freq. Control* **63** 1613–23

Dempsey R J *et al* 2018 Carotid atherosclerotic plaque instability and cognition determined by ultrasound-measured plaque strain in asymptomatic patients with significant stenosis *J. Neurosurg.* **128** 111–9

Drakopoulou M, Toutouzas K, Michelongona A, Tousoulis D and Stefanadis C 2011 Vulnerable plaque and inflammation: potential clinical strategies *Curr. Pharm. Des.* **17** 4190–209

Fernández-Ortiz A *et al* 2013 The progression and early detection of subclinical atherosclerosis (PESA) study: rationale and design *Am. Heart J.* **166** 990–8

Finn A V, Nakano M, Narula J, Kolodgie F D and Virmani R 2010 Concept of vulnerable/unstable plaque *Arterioscler. Thromb. Vasc. Biol.* **30** 1282–92

Fujikura K *et al* 2007 A novel noninvasive technique for pulse-wave imaging and characterization of clinically-significant vascular mechanical properties *in vivo Ultrason. Imaging* **29** 137–54

Garrard J *et al* 2015 Shear wave elastography may be superior to greyscale median for the identification of carotid plaque vulnerability: a comparison with histology *Ultraschall der Medizin—Eur. J. Ultrasound* **36** 386–90

Golemati S, Gastounioti A and Nikita K S 2013a Toward novel noninvasive and low-cost markers for predicting strokes in asymptomatic carotid atherosclerosis: the role of ultrasound image analysis *IEEE Trans. Biomed. Eng.* **60** 652–8

Golemati S, Lehareas S, Tsiaparas N N, Chatziioannou A, Nikita K S and Perrea D N 2013b Multiresolution features of carotid artery wall and plaque toward identifying vulnerable asymptomatic cases from B-mode ultrasound *2013 IEEE Int. Ultrasonics Symp. (IUS)* pp 872–5

Golemati S *et al* 2014 Toward recognizing the vulnerable asymptomatic atheromatous plaque from B-mode ultrasound: the importance of the morphology of the plaque shoulder *2014 IEEE Int. Ultrasonics Symp.* pp 2390–3

Grønholdt M L, Nordestgaard B G, Wiebe B M, Wilhjelm J E and Sillesen H 1998 Echo-lucency of computerized ultrasound images of carotid atherosclerotic plaques are associated with increased levels of triglyceride-rich lipoproteins as well as increased plaque lipid content *Circulation* **97** 34–40

Grotta J C 2013 Carotid stenosis *New Engl. J. Med.* **369** 1143–50

Hansen F, Mangell P, Sonesson B and Länne T 1995 Diameter and compliance in the human common carotid artery—variations with age and sex *Ultrasound Med. Biol.* **21** 1–9

Hansen H H G, de Borst G J, Bots M L, Moll F L, Pasterkamp G and de Korte C L 2016 Validation of noninvasive *in vivo* compound ultrasound strain imaging using histologic plaque vulnerability features *Stroke* **47** 2770–5

Hansen H H G, De Borst G J, Bots M L, Moll F, Pasterkamp G and De Korte C L 2013 Noninvasive compound ultrasound elastography for vulnerable plaque detection: *in vivo* validation *Eur. Heart J.* **34** P258

Hasegawa H, Hongo K and Kanai H 2013 Measurement of regional pulse wave velocity using very high frame rate ultrasound *J. Med. Ultrason.* **40** 91–8

Huang C, Su Y, Zhang H, Qian L-X and Luo J 2015 Pulse wave velocity measurement in healthy and diseased carotid arteries *in vivo 2015 IEEE Int. Ultrasonics Symp. (IUS)* pp 1–4

Huang C, Su Y, Zhang H, Qian L-X and Luo J 2016a Comparison of different pulse waveforms for local pulse wave velocity measurement in healthy and hypertensive common carotid arteries *in vivo Ultrasound Med. Biol.* **42** 1111–23

Huang R *et al* 2016b Detection of carotid atherosclerotic plaque neovascularization using contrast enhanced ultrasound: a systematic review and meta-analysis of diagnostic accuracy studies *J. Am. Soc. Echocardiogr.* **29** 491–502

Kruizinga P *et al* 2014 High-definition imaging of carotid artery wall dynamics *Ultrasound Med. Biol.* **40** 2392–403

Laurent S *et al* 2006 Expert consensus document on arterial stiffness: methodological issues and clinical applications *Eur. Heart J.* **27** 2588–605

Li R X *et al* 2018 Pulse wave imaging in carotid artery stenosis human patients *in vivo Ultrasound Med. Biol.* **45** 353–66

Li R X, Luo J, Balaram S K, Chaudhry F A, Shahmirzadi D and Konofagou E E 2013 Pulse wave imaging in normal, hypertensive and aneurysmal human aortas *in vivo*: a feasibility study *Phys. Med. Biol.* **58** 4549–62

Libby P, Ridker P M and Hansson G K 2011 Progress and challenges in translating the biology of atherosclerosis *Nature* **473** 317–25

Mcgarry M, Li R, Apostolakis I, Nauleau P and Konofagou E E 2016 An inverse approach to determining spatially varying arterial compliance using ultrasound imaging *Phys. Med. Biol.* **61** 5486–507

Mitchell C C *et al* 2017 Histopathologic validation of grayscale carotid plaque characteristics related to plaque vulnerability *Ultrasound Med. Biol.* **43** 129–37
Mitchell G F *et al* 2004 Changes in arterial stiffness and wave reflection with advancing age in healthy men and women *Hypertension* **43** 1239–45
Nadkarni S K, Bouma B E, de Boer J and Tearney G J 2009 Evaluation of collagen in atherosclerotic plaques: the use of two coherent laser-based imaging methods *Lasers Med. Sci.* **24** 439–45
Nagaoka R, Masuno G, Kobayashi K, Yoshizawa S, Umemura S and Saijo Y 2015 Measurement of regional pulse-wave velocity using spatial compound imaging of the common carotid artery *in vivo Ultrasonics* **55** 92–103
Nandalur K R, Hardie A D, Raghavan P, Schipper M J, Baskurt E and Kramer C M 2007 Composition of the stable carotid plaque *Stroke* **38** 935–40
Nandlall S D, Goldklang M P, Kalashian A, Dangra N A, D'Armiento J M and Konofagou E E 2014 Monitoring and staging abdominal aortic aneurysm disease with pulse wave imaging *Ultrasound Med. Biol.* **40** 2404–14
Nauleau P, Apostolakis I, McGarry M and Konofagou E 2018 Cross-correlation analysis of pulse wave propagation in arteries: *in vitro* validation and *in vivo* feasibility *Phys. Med. Biol.* **63** 115006
Negoita M, Hughes A D, Parker K H and Khir A W 2017 Non-invasive technique for determining local PWV in the human ascending aorta *Computing in Cardiology (CinC) 2017* pp 1–4
Ramnarine K V, Garrard J W, Kanber B, Nduwayo S, Hartshorne T C and Robinson T G 2014 Shear wave elastography imaging of carotid plaques: feasible, reproducible and of clinical potential *Cardiovasc. Ultrasound* **12** 49
Roy Cardinal M-H *et al* 2017 Carotid artery plaque vulnerability assessment using noninvasive ultrasound elastography: validation with MRI *Am. J. Roentgenol.* **209** 142–51
Saam T *et al* 2007 The vulnerable, or high-risk, atherosclerotic plaque: noninvasive MR imaging for characterization and assessment *Radiology* **244** 64–77
Saba L *et al* 2014 Imaging of the carotid artery vulnerable plaque *Cardiovasc. Intervent. Radiol.* **37** 572–85
van Popele N M *et al* 2001 Association between arterial stiffness and atherosclerosis: the Rotterdam study *Stroke* **32** 454–60
Vappou J, Luo J and Konofagou E E 2010 Pulse wave imaging for noninvasive and quantitative measurement of arterial stiffness *in vivo Am. J. Hypertens.* **23** 393–8
Widman E, Maksuti E, Larsson D, Urban M W, Bjällmark A and Larsson M 2015 Shear wave elastography plaque characterization with mechanical testing validation: a phantom study *Phys. Med. Biol.* **60** 3151–74